CRYSTAL GROWTH & DESIGN

pubs.acs.org/crystal

Article

Effect of Porous and Nonporous Polycaprolactone Fiber Meshes on $CaCO_3$ Crystallization Through a Gas Diffusion Method

Felipe Sepúlveda, Nicole Butto, José Luis Arias, Mehrdad Yazdani-Pedram, Piotr K. Szewczyk, Adam Gruszczynski, Urszula Stachewicz, and Andrónico Neira-Carrillo*

Cite This: *Cryst. Growth Des.* 2020, 20, 5610−5625

Read Online

ACCESS | Metrics & More | Article Recommendations | Supporting Information

ABSTRACT: The effect of nonporous (NP-PCL) and porous (P-PCL) fibrous polycaprolactone (PCL) meshes, used as templates, on *in vitro* $CaCO_3$ crystallization via a gas diffusion (GD) method at 20 °C for 24 h was studied. The nonporous random (NPR-PCL) and porous random (PR-PCL) and the nonporous-aligned (NPA-PCL) and porous-aligned (PA-PCL) fibrous PCL meshes were directly spun on flat or rotary collectors from 18% PCL solutions using ethyl acetate/acetone or ethyl acetate/dimethyl sulfoxide, respectively. The morphology and type of $CaCO_3$ crystal grown on PCL fiber scaffolds were analyzed by Fourier transform infrared spectroscopy (FTIR), contact angle measurements, scanning electron microscopy coupled with energy dispersive X-ray spectroscopy (SEM-EDS), focused ion beam combined with scanning electron microscopy (FIB-SEM), and X-ray diffraction (XRD) techniques. The PCL fibers distributions affected the nucleation and stabilized calcite and vaterite polymorphs of $CaCO_3$ with different crystal population densities. The crystal density of vaterite was higher than calcite (2:1) when the NPA-PCL and PA-PCL fibers were used as a template, but calcite predominated (2:1) on P-PCL fiber mesh with respect to the NP-PCL fiber mesh. We found that $CaCO_3$ crystals covered the surface of PCL fibers, and some of them grown from inside of the PCL fibers showed that PCL fibers were occluded inside the $CaCO_3$ crystals during the GD crystallization. The nano- and microscale topological features of PCL scaffolds control the diffusion of carbon dioxide (CO_2) gas through PCL fiber meshes in the soaking of PCL meshes into a calcium chloride ($CaCl_2$) solution during the GD crystallization affecting subsequently the nucleation and growth of $CaCO_3$ crystals. Indeed, pore size feature of the micrometric A-PCL and nanometric R-PCL fiber meshes affected the intensities of the crystallographic faces of calcite and vaterite as observed by XRD. Contact angle measurements of the aqueous and crystallization liquid droplet on NPR-PCL, PR-PCL and A-PCL fibrous showed different hydrophobic character of the PCL meshes. This study shows the role of the nano- and microscale topological features and the presence of pores on PCL fiber scaffolds on the mineralization behavior of $CaCO_3$ deposited on R-PCL and A-PCL fiber scaffolds, and by this approach various aspects of controlled $CaCO_3$ crystallization such as nucleation and crystal growth of biomaterials based on $CaCO_3$ can be studied with potential biotech applications.

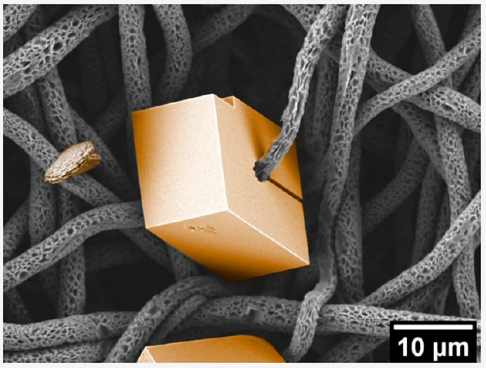

1. INTRODUCTION

Biomineralization is the process by which living organisms form hierarchical hybrid biogenic minerals termed biominerals.[1−3] Biominerals are spontaneously produced through a *bottom-up* process and play a key role, including protection, motion, storage, optical and gravity sensing, defense, detoxification, among others.[4−6] There is a large diversity of chemical compositions of biominerals such as carbonates, silicates, phosphates, oxides, among others.[7,8] They are highly organized from the molecular level to the nano- and macroscale with intricate nanoarchitectures that ultimately make up a myriad of different functional soft and hard tissues.[9,10] The unique properties of biominerals can inspire mimetic strategies intended to design materials based on mineral controlled crystallization for new advanced technologies. Indeed, chemists are inspired by the underlying molecular processes and aim to mimic *in vitro* biological crystallization and to transfer them to modern biocomposite materials.[11−13] This process is strictly controlled by organic macromolecules such as proteins and polysaccharides acting as templates.[14]

Calcium carbonate ($CaCO_3$) is the most studied biomineral, which can facilitate the understanding of the crystallization process and the control of biomineralization.[15,16] $CaCO_3$ biominerals consist of single crystals

Received: June 11, 2020
Revised: June 22, 2020
Published: June 30, 2020

https://dx.doi.org/10.1021/acs.cgd.0c00803
Cryst. Growth Des. 2020, 20, 5610−5625

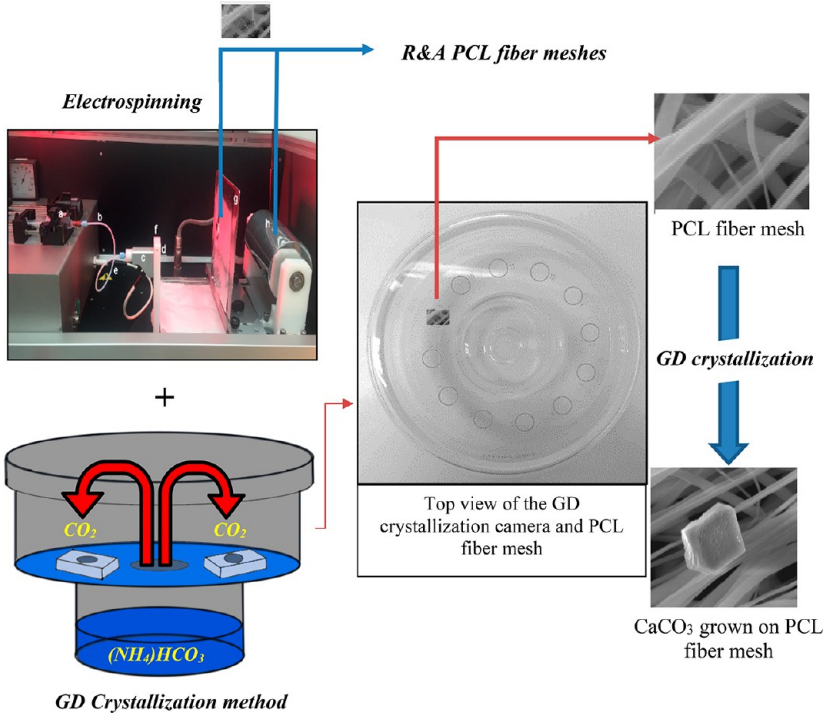

Figure 1. GD crystallization setup of $CaCO_3$ on electrospun PCL fibers.

intimately associated with organic macromolecular matrices. $CaCO_3$ typically contains a small amount of ca. 0.1−1.0 wt % acidic proteins, such as aspartic acid-rich proteins and acidic macromolecules that can control the nucleation and crystal growth.[17] In fact, toughness, solubility, and the shape of biominerals influence the degree of crystallization and the type of minerals.[1−5,18,19] There are three polymorphs of anhydrous $CaCO_3$, which differ in size, morphology, and stability; these are calcite, aragonite, and vaterite, listed in order of decreasing thermodynamic stability.[20] Calcite and aragonite represent the main mineral phases among the marine biogenic $CaCO_3$.[21] Aragonite and calcite are thermodynamically more stable structures, and they often occur in nature. Vaterite can rapidly transform to calcite and aragonite in aqueous solution.[22]

It is known that in nature organic macromolecular matrices are commonly used as templates, i.e., soluble and insoluble matrices, where the shape, e.g., platelet or fibers, exerts control over the *in vitro* crystallization of mineral regulating the nucleation, morphology, polymorphism, crystallographic orientation, confined nucleation space, and the final mineral deposition.[23−25] Biominerals are valuable materials not only for understanding the biomineralization but also for novel confined-materials synthesis and design, which avoids undesirable pathological biomineralization.[26,27] The inspiration from biomineralization is of great interest to materials scientists who seek novel materials syntheses with fibrillary hydrogel structures and interfaces based on analogous crystalline forms to those formed by nature.[11,12,28] Bio-inspired morphosynthesis emerged as a novel and environmentally friendly route to generate superior materials with controlled morphologies through organic self-assembled structures or by using functionalized polymeric templates.[29] In this regard, electrospun fibers of synthetic and natural polymers as scaffolds for design of tissue engineering materials have been utilized.[30] The use of electrospun polycaprolactone (PCL) fiber as a template for crystallization of $CaCO_3$ using ultrasonic treatment has been reported by Savelyeva et al. in 2017 where porous vaterite covering the PCL fiber surface was obtained.[31] Recently, the mineralization behavior of $CaCO_3$ deposited on randomly oriented fibers of PCL scaffolds, previously treated with low-temperature plasma, has been studied. The authors confirmed that preferential growth of the vaterite occurred in the O_2-plasma-treated PCL scaffold. They tried to improve the wettability and permeability of PCL scaffolds for obtaining a superior hybrid composite coated with highly porous $CaCO_3$, which is a prerequisite for biomedical scaffolds used for drug delivery and biosensors.[32,33] It is well-known that the morphology, size, and type of $CaCO_3$ crystals are controlled not only by the crystallization method but also by the variation of experimental parameters such as the concentration of the template, molar ratio of the reactants, pH, temperature, time, among others.[34−36] Despite the above, the effects of topography and porosity on electrospun PCL fibers used as an organic template on the *in vitro* $CaCO_3$ crystallization via a gas diffusion (GD) method are still unknown. With this background in mind, we believe that the use of organic 3D fibrillar PCL meshes as a template having different topography, with or without micro-/nanopore on the surface, may allow the control of the nucleation and type of $CaCO_3$ crystals. It is known that the roughness is intimately related to the porosity of the solid substrate.

We report a further advancement of the micro-/nano-topography effect of nonporous and porous electrospin of R-PCL and A-PCL fiber meshes on the *in vitro* crystallization of $CaCO_3$ via the GD method at 20 °C for 24 h. The GD method is an excellent *in vitro* crystallization method for evaluating the effect of additives and solid substrates in crystalline nucleation as demonstrated by using an eggshell membrane[37] on the top of a microbridge container with the mammillary side facing up and upside down based on the

https://dx.doi.org/10.1021/acs.cgd.0c00803
Cryst. Growth Des. 2020, 20, 5610−5625

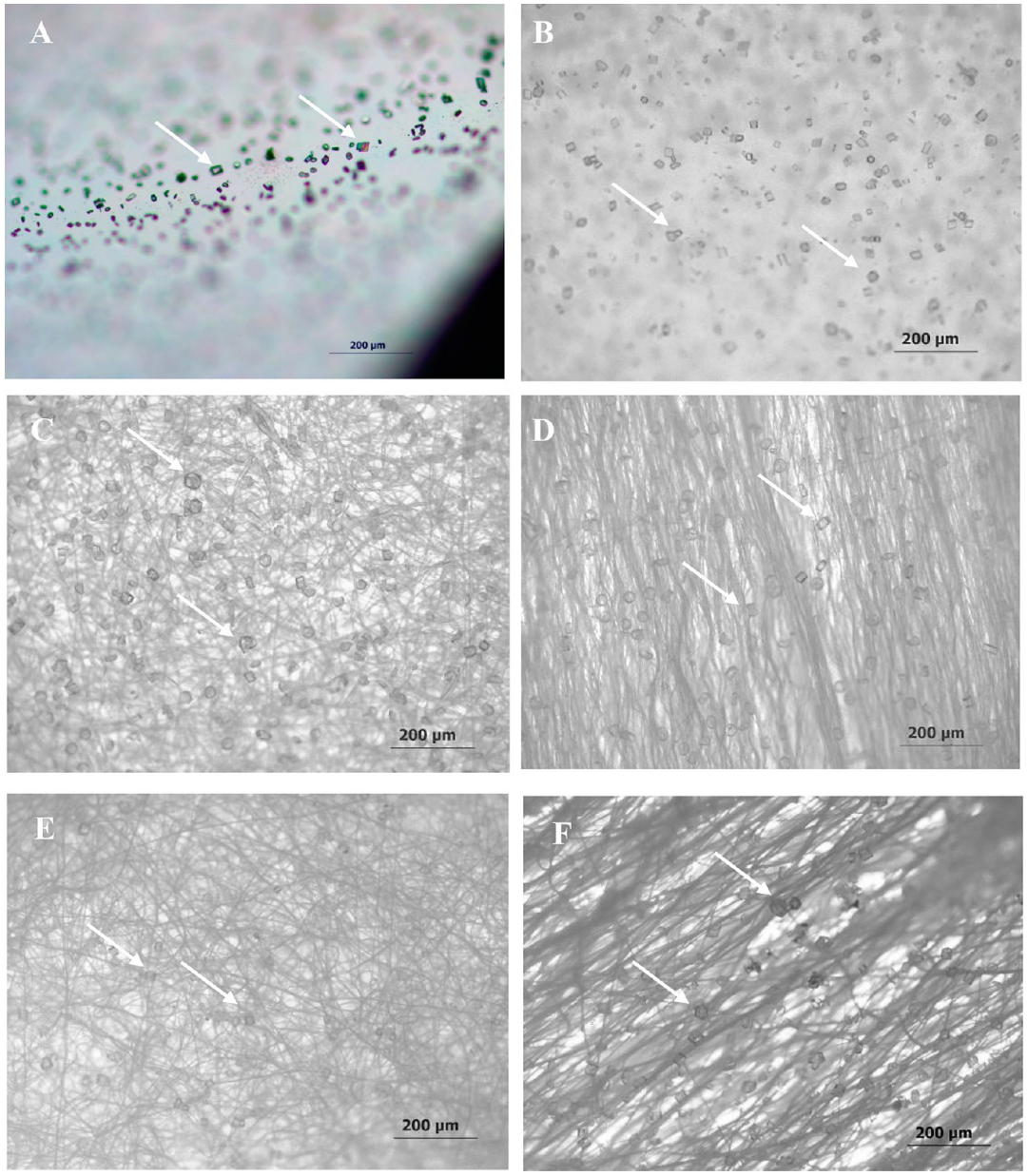

Figure 2. Optical images of $CaCO_3$ crystals grown on the surface of (A) glass substrate, (B) melted PCL, (C) R-PCL fibers mesh, (D) A-PCL fibers mesh, (E) PR−PCL fibers mesh, and (F) PA−PCL fibers mesh. Magnification 10×. The white arrows indicate the presence of some crystals.

variation of the sitting drop method developed by Dominguez-Vera et al. 2000.[38] The topography and the distribution of the PCL fibers were achieved by using flat or rotating collectors in electrospinning. The morphology of PCL fibers, type, and polymorphism of $CaCO_3$ were analyzed by scanning electron microscopy, FTIR spectroscopy, and X-ray diffraction techniques. We demonstrated that the nano- and microscale topological features of PCL fiber meshes and the presence of pores on the fiber surface used as template affect the mineralization behavior of $CaCO_3$, which renders the possibility of using anionic PCL fiber scaffolds such as carboxylate and sulfonate functional groups as an active mineralization template. We also describe and discuss how the distribution of R-PCL and A-PCL fibers and the presence of pores on the PCL fibers surface enable the stabilization of calcite and vaterite polymorphs affecting the crystal density predominance and their crystallographic faces.

2. EXPERIMENTAL SECTION

2.1. Materials and Chemicals. A detailed description of the materials, chemical reagents, and preparation of the R-PCL and A-PCL fibers meshes is available in the Supporting Information.

2.2. Gas Diffusion (GD) Crystallization of $CaCO_3$. *In vitro* GD crystallization of $CaCO_3$ was performed on pieces of PCL electrospun fiber meshes (2 × 3 mm) at 20 °C for 24 h. Similar *in vitro* GD experiment crystallization has been reported.[14,25,39−41] GD crystallization setup, solution preparation, and washing protocols, performed to remove any floating crystals formed in the $CaCl_2$ solution that could be deposited on the PCL fiber meshes, are provided in the Supporting Information (Figure S1).

2.3. Electrospun Meshes of PCL. A-PCL and R-PCL fibers meshes with and without pores were obtained from 18% (w/v) PCL solution prepared using ethyl acetate/acetone 3:1 (v:v) solution with

https://dx.doi.org/10.1021/acs.cgd.0c00803
Cryst. Growth Des. 2020, 20, 5610−5625

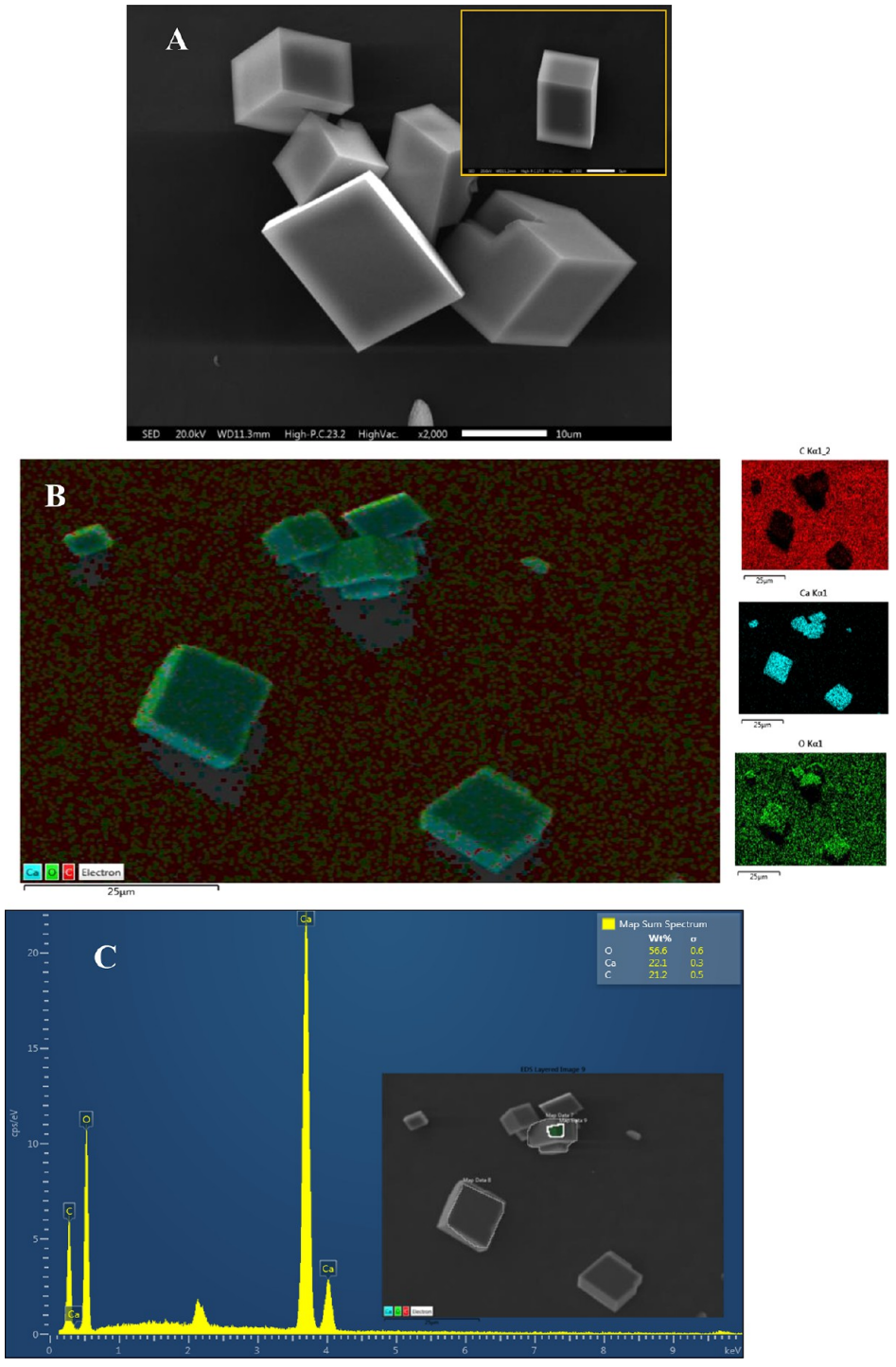

Figure 3. SEM-EDX of $CaCO_3$ crystals grown on the surface of melted PCL. (A) Calcite crystals, (B) EDX spectra of calcium, carbon, and oxygen elements of calcite crystal grown on melted PCL, (C) EDX spectra of elemental chemical composition of calcite crystals (*).

flat or rotating collectors, respectively. P-PCL meshes from 18% PCL solution in ethyl acetate/DMSO 1:9 (v:v) solution were prepared. For all the solvents investigated for electrospinning of PCL fibers, PCL (M_w = 80 000 g/mol) in an eStretching LE-10 Fluidnatek equipment was utilized. Preparation of all PCL fiber meshes, electrospinning process parameters, and ambient conditions are also provided in Supporting Information (Figure S2).

2.3.1. Characterization. A few characterization techniques were utilized in order to provide surface and physicochemical characterization of PCL meshes and $CaCO_3$ crystals according to the experimental GD crystallization method for $CaCO_3$ production on A-PCL and R-PCL fiber meshes (Figure 1). The surface morphology and microanalysis of the resultant $CaCO_3$ crystals were observed by scanning electron microscopy (SEM) coupled with energy dispersive X-ray (EDX) analysis. The fiber diameter measurements were also presented in the form of histograms. The crystal density predominance was determined based on the number of crystal population of vaterite and calcite crystals accounted for by using a lower magnification field at 70×. The SEM-EDX measurements were performed by using a SEM (JEOL JSM-IT300LV, JEOL USA Inc., USA) connected to an EDX detector for elemental analysis with computer-controlled software, the Aztec EDX system (Oxford Instruments, Abingdon, UK). In addition, cross-sectional imaging of the $CaCO_3$ crystals grown on the

https://dx.doi.org/10.1021/acs.cgd.0c00803
Cryst. Growth Des. 2020, 20, 5610−5625

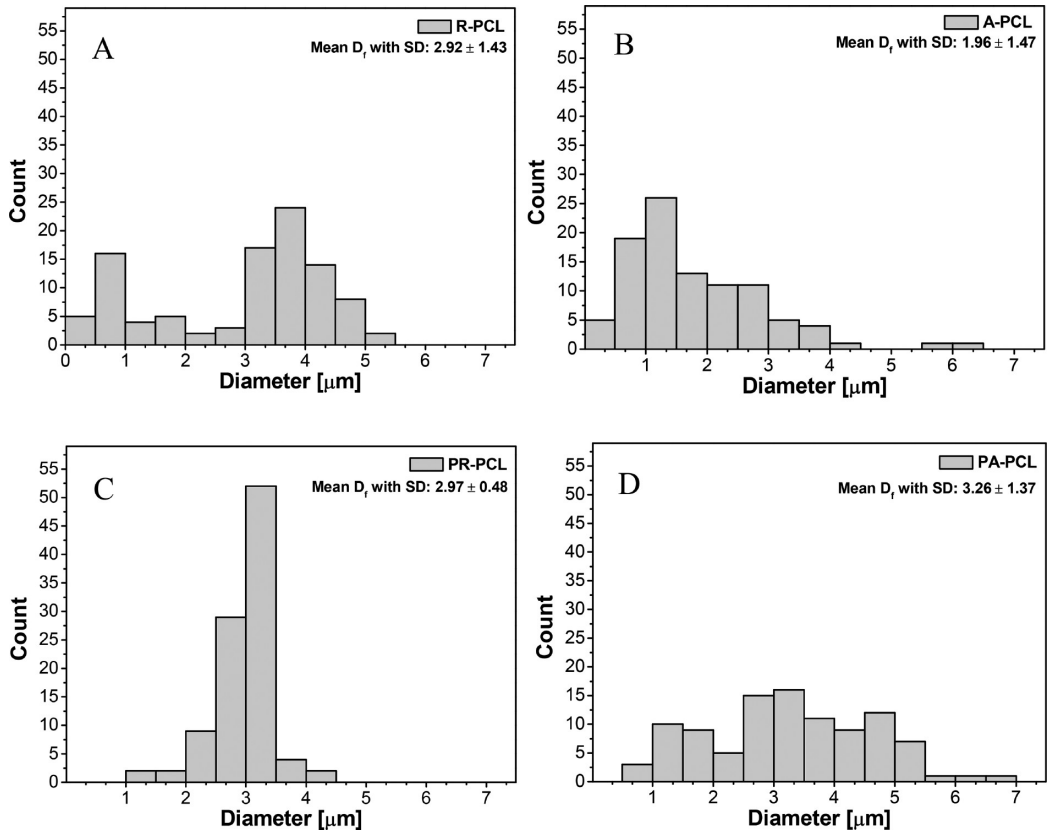

Figure 4. Histogram of the fiber diameter distribution of PCL electrospun fiber meshes used as a template for *in vitro* $CaCO_3$ GD crystallization performed at 20 °C for 24 h. (A) R-PCL, (B) A-PCL, (C) PR-PCL, and (D) PA-PCL.

electrospun PCL fiber mesh was achieved using a dual beam system with focus ion beam (FIB) and SEM (NEON CrossBeam 40EsB, ZEISS, Germany). Prior to the imaging, the samples were coated with 5 nm gold layer using rotary-pumped sputter coating (Q150RS, Quorum Technologies, UK). FIB was performed using a Ga^+ ion beam current of 5 nA and voltage of 30 kV. The sample stage was tilted so that the sample surface was perpendicular to the FIB direction and 52° incidents to the electron beam.[42,43] The images of cross-sectioned fibers were taken by SEM at a current of 500 pA and voltage of 5 kV. Water and crystallization solution ($CaCl_2$ in TRIS buffer pH 9.00) contact angle [°] measurements were performed by the DataPhysis optical contact system OCA 15EC (DataPhysics instruments GmbH, Filderstad, Germany) on melted PCL, glass, nonporous and porous electrospun R-PCL and A-PCL fiber mesh surfaces. The dosing volume was performed at 10 μL. The resulting average values is reported with the standard deviation (±SD). The method of measuring contact angles on PCL surface is provided in Supporting Information (Figure S3). The Fourier transform infrared spectroscopy-attenuated total reflection (FTIR-ATR) analyses of the PCL fiber meshes were performed to characterize all PCL polymer meshes and starting polymer materials by using an Interspectrum Interspec p/n 200-X instrument. The specific surface area analysis of the different PCL meshes used as template was measured by the nitrogen (N_2) method of Brunauer–Emmett–Teller (BET). Analysis of an N_2 adsorption/desorption isotherm at 273.0 K using an outgas time of 1.0 h and analysis time between 119.8 to 137.7 min in an automatic analyzer (Quantachrome Nova Station A) instrument. Powder X-ray diffraction (PXRD) of the $CaCO_3$ crystals was carried out by using a Siemens D-5000X X-ray diffractometer with Cu–Kα radiation (graphite monochromator) and an ENRAF Nonius FR 590. The crystal structure of CaOx was determined by using Cu–Kα radiation (40 kV), step sizes of 0.2°, and the geometric Bragg–Brentano (θ–θ) scanning mode with an angle (2θ) range of 5–70°. The DiffracPlus program was used as the data control software.

3. RESULTS AND DISCUSSION

FTIR analysis was used to characterize all starting PCL solutions before electrospinning and the random (R-PCL) and aligned (A-PCL) electrospun PCL fiber meshes, and the PCL film as a control. All PCL fiber meshes showed the characteristic spectroscopic pattern for PCL in which the stretching vibrations of the C═O bond in the region of 1727 cm^{-1} was present, as already described by Shoja et al.[44] FTIR spectra of nonporous and porous electrospun R-PCL and A-PCL fiber meshes, melted PCL film as a control template, and the 18% PCL solution in ethyl acetate/DMSO 1:9 (v:v) and ethyl acetate/acetone 3:1 (v:v) solutions before the electrospinning process for the formation of porous and nonporous random PCL fiber meshes are provided in Supporting Information (Figure S4).

The mineralization of $CaCO_3$ using GD crystallization in the presence of different PCL fiber meshes resulted in particles with different $CaCO_3$ crystal structures and morphologies. The formation and crystals grown of $CaCO_3$ at the surface of PCL fibers were preliminary visualized through optical microscopy (Figure 2). The formation of abundant $CaCO_3$ particles on the glass substrate and melted PCL surfaces both used as controls (Figure 2A,B) and on the four variants of PCL fiber meshes used as 3D templates (Figure 2C–F) was demonstrated. Although conventional optical microscopy has poor resolution and it is difficult to notice in detail any morphological features and to identify the type of $CaCO_3$ crystals, in the current study this technique

https://dx.doi.org/10.1021/acs.cgd.0c00803
Cryst. Growth Des. 2020, 20, 5610–5625

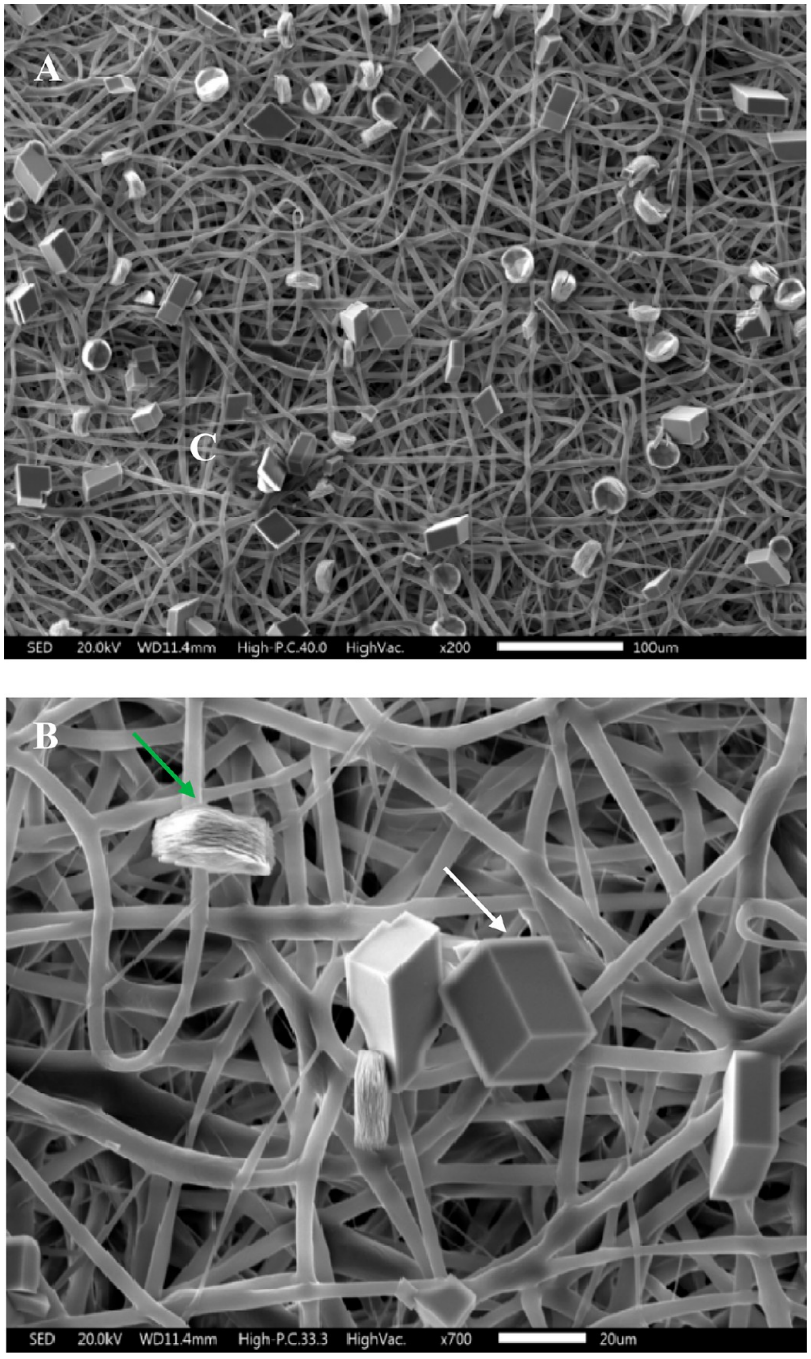

Figure 5. SEM images of $CaCO_3$ crystals grown on the surface of R-PCL mesh. (A) General view showing abundant crystals, (B) calcite and vaterite crystals. The white and green arrows indicate calcite and vaterite crystals, respectively.

represents the simplest and fast imaging tool to show the presence of crystals and the $CaCO_3$ distribution of the electrospun PCL fiber meshes.

In addition, similar observation was performed by using SEM-EDX analysis. Figure 3 shows the SEM-EDX of $CaCO_3$ crystals grown on the surface of melted PCL and the elemental chemical composition of the resultant crystals grown on it. Figure 3A,B shows the morphology of the typical rhombohedral calcite with smooth edges obtained by using melted PCL (negative control) and the EDX of calcium (Ca), carbon (C), and oxygen (O) elements of calcite and the surface of melted PCL template, respectively. We notice that melted PCL film did not affect the $CaCO_3$ morphology. Figure 3C shows that the weight percent (wt %) of the individual Ca, C, and O elements located in the flat area (* in image) of the calcite surface, automatically calculated by the EDX software, demonstrated a good correspondence to the theoretical Ca/O ratio of 1:3 of pure calcite surface.

With this in mind, a set of *in vitro* GD crystallizations of $CaCO_3$ was carried out to evaluate the effect of both random and oriented PCL and the nonporous and porous-PCL fiber meshes (2 × 3 mm) as a template on the nucleation and crystal growth of $CaCO_3$. Figure 4 shows the histogram of the fiber diameter distribution of PCL electrospun fiber meshes of R-PCL (Figure 4A), A-PCL (Figure 4B), PR-PCL

https://dx.doi.org/10.1021/acs.cgd.0c00803
Cryst. Growth Des. 2020, 20, 5610−5625

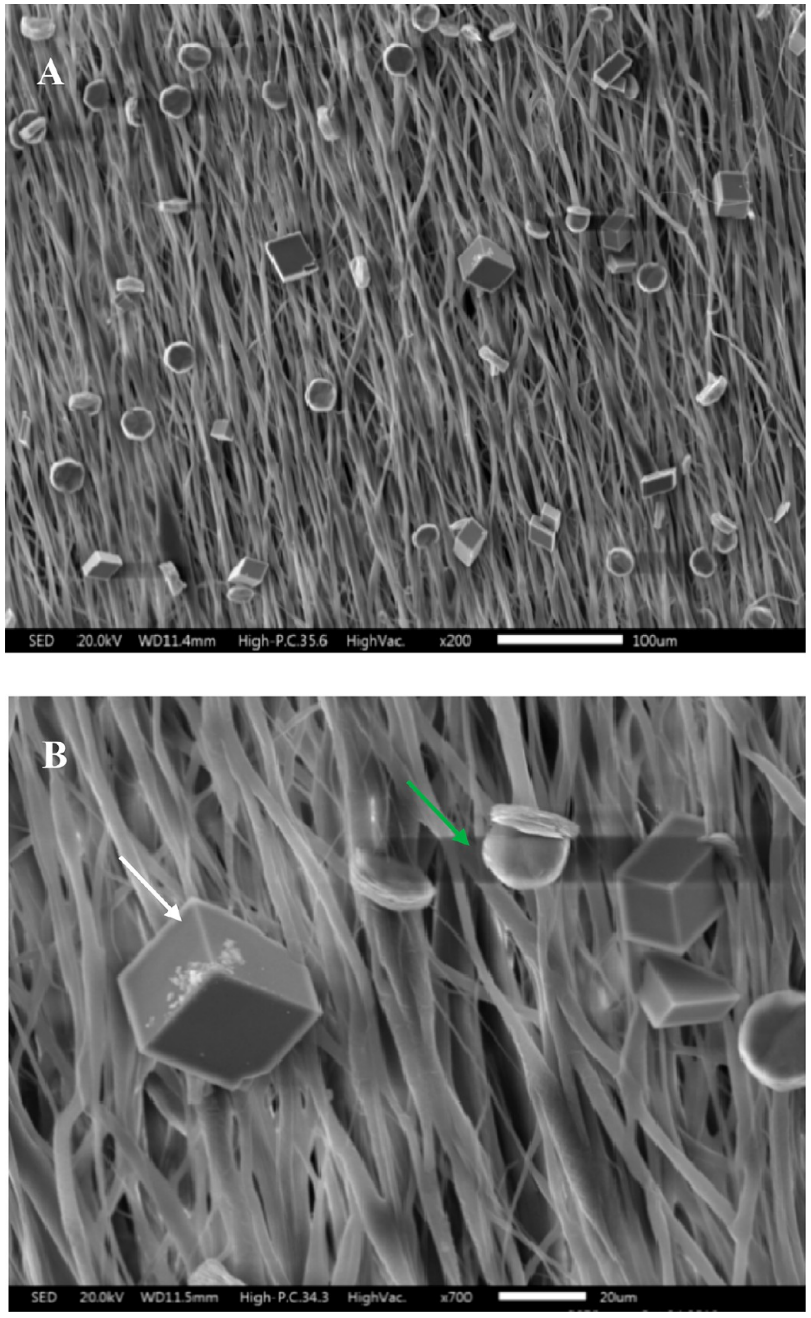

Figure 6. SEM images of $CaCO_3$ crystals grown on the surface of A-PCL mesh. (A) General view showing abundant crystals, (B) calcite and vaterite crystals. The white and green arrows indicate calcite and vaterite crystals, respectively.

(Figure 4C), and the PA-PCL (Figure 4D) polymer meshes performed at 20 °C for 24 h.

Figures 5 and 6 show the SEM images of $CaCO_3$ crystals grown on the surface of NPR-PCL and NPA-PCL meshes, respectively.

In general, Figures 5 and 6 show two types of $CaCO_3$ crystals corresponding to calcite and vaterite polymorphs obtained in the presence of nonporous electrospun R-PCL and A-PCL fiber meshes. The random and aligned NP-PCL fiber meshes allow the formation of the nonagglomerated rhombohedral calcite and oval shape of vaterite in all GD crystallization essays. Our experimental finding indicates that when R-PCL fiber meshes were used as a template (Figure 5) the crystal population densities of calcite and vaterite were 1:1 and the size for the calcite was between 22 and 25 μm and for vaterite the sizes varied between 21 and 28 μm, respectively. However, when the A-PCL fiber meshes was used as a template (Figure 6), the crystal population densities of calcite and vaterite changed to 1:2, and the size for the calcite and vaterite was ca. 20.0 μm. The average diameter of electrospun fibers was ca. 4.3 and 3.4 μm for R-PCL and A-PCL fiber meshes, respectively. In general, nonagglomerated crystals particles were found, and we observed that the $CaCO_3$ crystals were covered by PCL fibers (Figure 7A,B), and we rarely observe crystals grown surrounding PCL fibers showing that fibers were occluded inside the crystals (Figure 7C,D) during the GD crystallization as is illustrated in Figure 7.

In order to know if electrospun scaffold pore size and PCL fibers distributions play a significant role in the $CaCO_3$

https://dx.doi.org/10.1021/acs.cgd.0c00803
Cryst. Growth Des. 2020, 20, 5610−5625

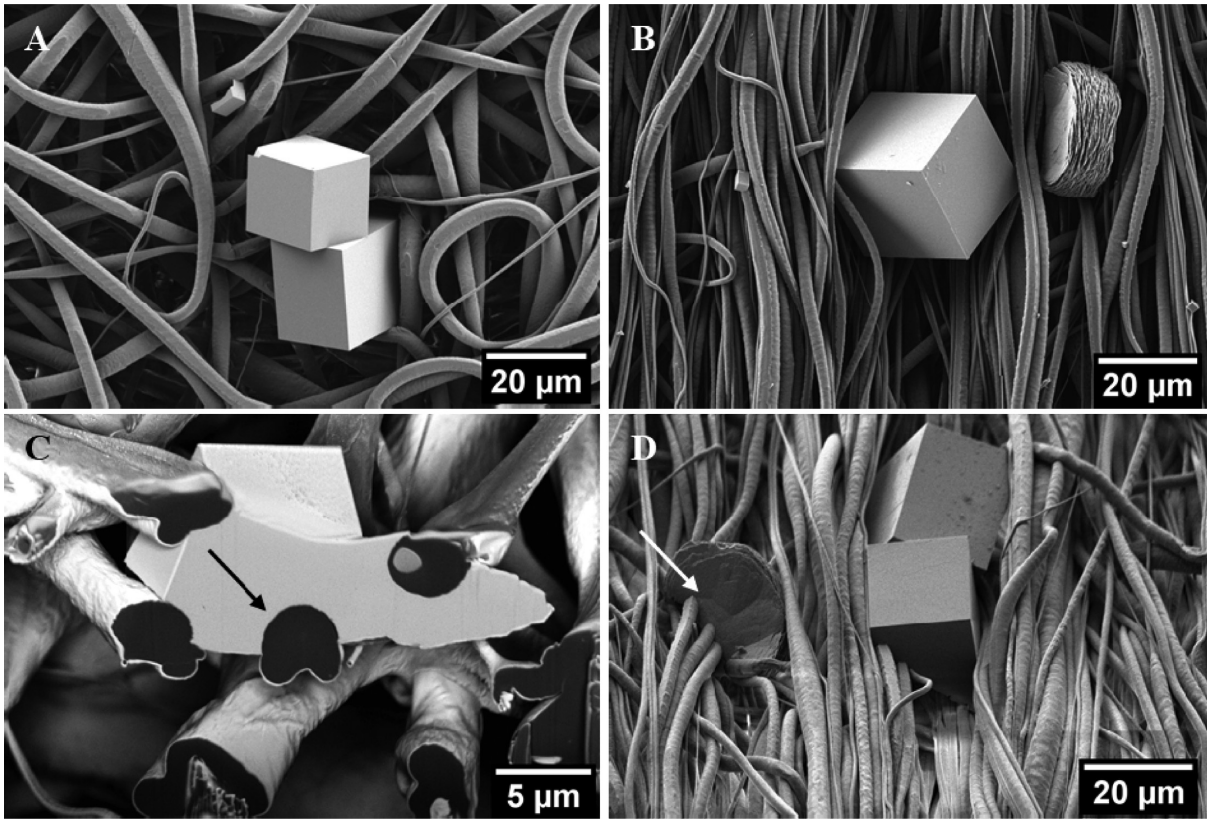

Figure 7. SEM images of $CaCO_3$ crystals grown on the (A, B) surface and surrounding (C, D) on R-PCL and A-PCL meshes. The black and white arrows indicate how calcite and vaterite crystals are interpenetrated by PCL fibers, respectively.

nucleation behavior, stabilization of calcite and vaterite polymorphs, and crystal population densities, a set of GD crystallizations of $CaCO_3$ utilizing pieces of PR-PCL and PA-PCL electrospun fiber meshes (2 × 3 mm) was also performed. Figures 8 and 9 show the SEM images of $CaCO_3$ crystals grown at the surface of porous electrospun R-PCL and A-PCL fiber meshes, respectively.

The pores size of the electrospun PCL scaffolds and its fibers distributions analyzed by SEM had a noteworthy influence on the population densities of calcite and vaterite polymorphs, size of crystals, average diameter of electrospun fibers, and the presence of agglomerated crystals precipitation. Figure 8 shows that the population densities of calcite and vaterite were 2:1, and the size for the calcite was ca. 13.5 μm and for vaterite the size was ca. 11.8 μm, respectively. However, when the PA-PCL fiber meshes were used as template (Figure 9) the population densities of calcite and vaterite was 2:1 and the size for the calcite was ca. 23 μm, and for vaterite the sizes was ca. 18.5 μm, respectively. In SEM analysis, the size scaling of the images allows us to determine the average diameter of electrospun fibers directly, these being ca. 2.4 and 4.5 μm and for the average pore size of PCL fibers values of 203 nm and 1.00 μm for the PR-PCL and PA-PCL fiber meshes, respectively. We notice that the phenomena of particle agglomeration were present, and we also observed that $CaCO_3$ crystals were covered by PCL fibers. In addition, some crystals are being pierced by a porous random PCL fiber as illustrated in Figure 10.

On the other hand, SEM-EDX spectra and elemental chemical composition of calcite and vaterite grown on R-PCL (Figure 11) and A-PCL (Figure 12) fiber meshes were also obtained. Figure 11 shows the SEM-EDX of calcite and vaterite grown on R-PCL fibers mesh (Figure 11A) and the major-elements composition of $CaCO_3$, that is, carbon (C), calcium (Ca), and oxygen (O) (Figure 11B). EDX analysis was carried out in order to determine the Ca/C/O ratio for different $CaCO_3$ polymorphs and compare them with the theoretical Ca/C/O ratio of 1:1:3 pure $CaCO_3$. We observed that Ca is distributed only in the crystalline particles confirming the identification of $CaCO_3$, while the C and O elements were present in all selected area. The weight percentages of Ca, C, and O were found as 3.2%, 33.0%, and 63.8%, respectively, which correspond to a nonstoichiometric yielding of Ca/C/O ratio ca. of 1:10:20. We believe that the elemental chemical mapping of these two elements is considered both the inorganic particles and the organic component. In this regard, when the melted PCL film was used as a solid template (see Figure 3), the wt % of Ca, C, and O was 22.1%, 21.2%, and 56.6%, respectively, corresponding to a Ca/C/O ratio of 1:1:2.6, which is close the theoretical 1:1:3 ratios. SEM-EDX of individual calcite and vaterite polymorphs grown on aligned PCL fiber mesh was also analyzed (Figure 12). Here, the wt % of Ca, C, and O for calcite was 19.6%, 28.5%, and 51.9%, respectively, corresponding to a Ca/C/O ratio of 1:1.5:2.6 (Figure 12A). In the case of vaterite, the wt % of Ca, C, and O was 22.7%, 24.2%, and 53.1%, respectively corresponding to a Ca/C/O ratio of 1:1:2.3 (Figure 12B). This observation allows to suggest that the stoichiometry of calcite and vaterite crystals changes very slightly with respect to their theoretical stoichiometry of pure polymorphs, and the stabilization of both polymorphs could be controlled by attaching functional

https://dx.doi.org/10.1021/acs.cgd.0c00803
Cryst. Growth Des. 2020, 20, 5610−5625

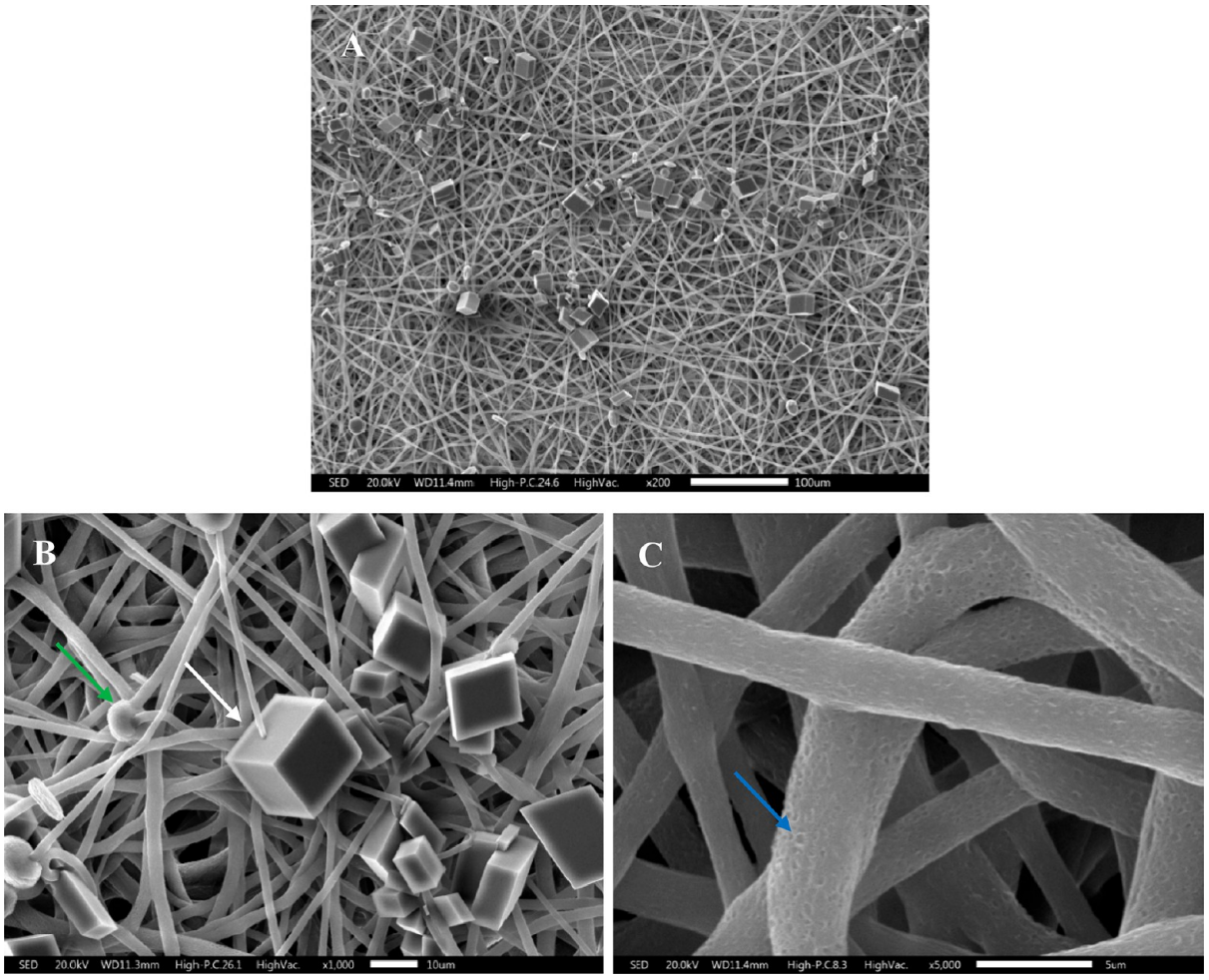

Figure 8. SEM images of $CaCO_3$ crystals grown on the surface of PR-PCL mesh. (A) General view showing abundant crystals, (B) calcite and vaterite crystals, and (C) porous surface of PCL fibers. The white and green arrows indicate how calcite and vaterite crystals are interpenetrated by PCL fibers, respectively. The blue arrows show pores on the surface of the PCL fiber.

groups on the surface, which could depend on pore size, surface area, and hydrophobic character of the PCL surface-meshes.

In order to determine the hydrophobic/hydrophilic character of all electrospun PCL meshes, ultrapure water and crystallization solution ($CaCl_2$ in TRIS buffer pH 9.00) contact angle [°] measurements on PCL fiber surface were performed. The method of measuring and angles stock images on PCL surface is provided in Figure S3. Table 1 shows the contact angle [°] values for random and aligned PCL fibers mesh surfaces, glass substrate, and melted PCL surface. In general, we found that all electrospun PCL meshes behave as low wettability systems with respect to both controls, which presented values less than 90°. Moreover, in the case of the NP-PCL scaffolds system, the A-PCL fibers showed a greater contact angle than R-PCL fibers (115.88 ± 1.26°/104.06 ± 2.92°) showing the effect of roughness on the wetting. Since it is known that the porosity of a solid substrate is intimately related to the roughness,[45] in the case of P-PCL scaffolds systems, the PA-PCL fibers presented a smaller contact angle than PR-PCL fibers (113.53 ± 1.71°/119.31 ± 1.50°) in aqueous liquid, probably due to a larger pore size (ca. 1.00 μm), which were five times larger than of the P-PCL fiber system with a random distribution of fibers. Therefore, we observed that the intrinsically hydrophilic PCL surface could be altered by creating topographical patterns through PCL fibers distribution.[46] The presence of micro-/nanopore on PCL fibers surface affects the nucleation and crystal growth of $CaCO_3$. In general, the hydrophilic/hydrophobic nature of the electrospun PCL substrate changed according to the different contact angle values in the aqueous and liquid crystallization media; however, the contact angle of the PA-PCL mesh did not change in both liquid media. By comparing the contact angle measurements between the NPR-PCL and NPA-PCL meshes, the aligned orientation of fibers always had a higher contact angle and therefore a greater hydrophobic character attributed. However, between the PR-PCL and PA-PCL meshes, the contact angle on R-PCL fiber mesh was higher, in fact, reaching the highest contact angle values in water and crystallization media. Thus, the surface wettability of polymer material is of great relevance since it determines the degree of infiltration of $CaCO_3$ crystals in polymeric meshes, where the greater hydrophilic character of the meshes results in a greater infiltration of crystals.[47]

In addition to the SEM observations of electrospun PCL fiber meshes, the surface area measurements (BET technique) on PCL fiber meshes could indicate the pore size, CO_2 gas diffusion through the electrospun PCL substrate, and represents a suitable surface characterization

https://dx.doi.org/10.1021/acs.cgd.0c00803
Cryst. Growth Des. 2020, 20, 5610−5625

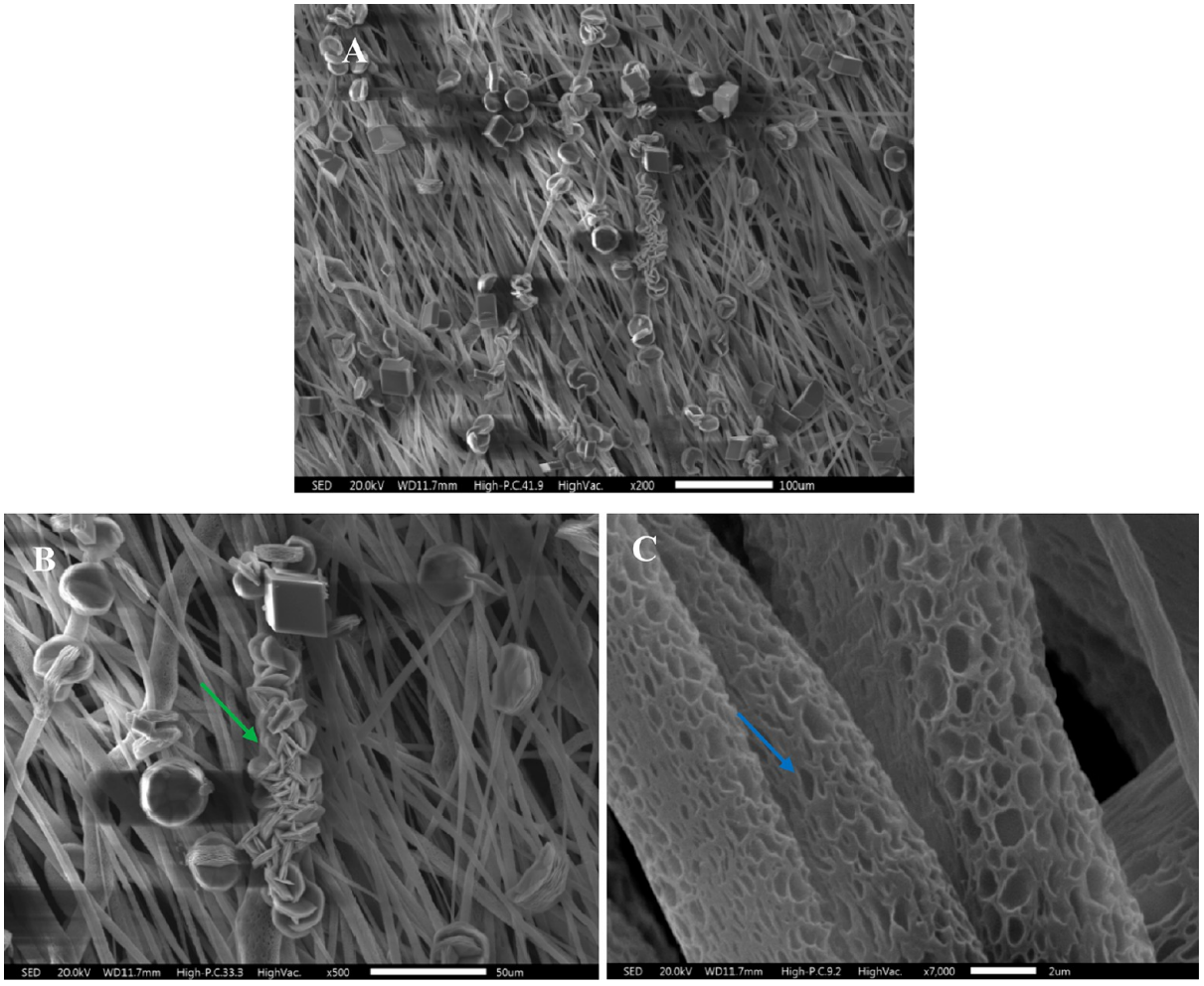

Figure 9. SEM images of $CaCO_3$ crystals grown on the surface of PA-PCL mesh. (A) general view showing abundant crystals, (B) calcite and vaterite crystals, and (C) porous surface of PCL fibers. The green arrow indicates agglomerated vaterite crystals in (B), and blue arrow shows pores on the surface of the PCL fiber in (C).

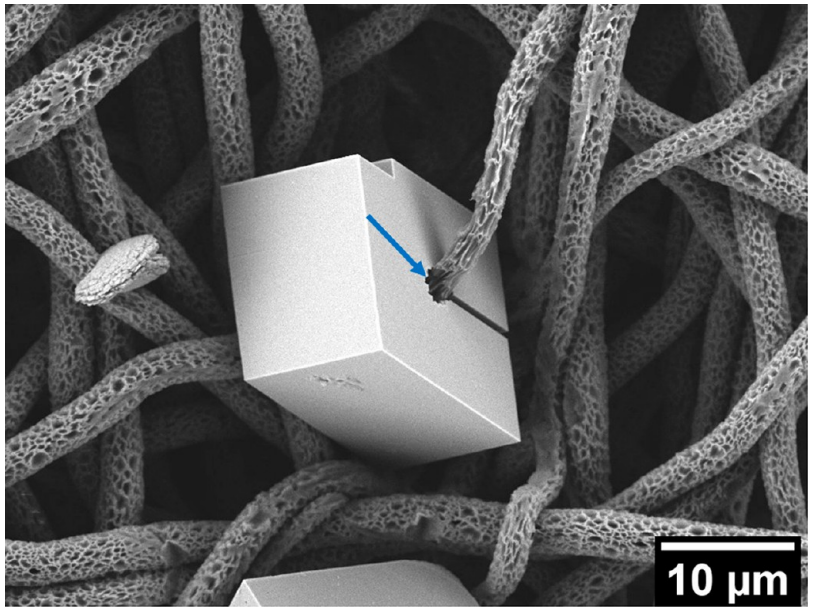

Figure 10. SEM image of a calcite crystal being pierced by a PR-PCL fiber. The blue arrow shows pores on the surface of the PCL fiber and how calcite is clearly pierced in the middle of the crystal by a porous PCL fiber.

https://dx.doi.org/10.1021/acs.cgd.0c00803
Cryst. Growth Des. 2020, 20, 5610−5625

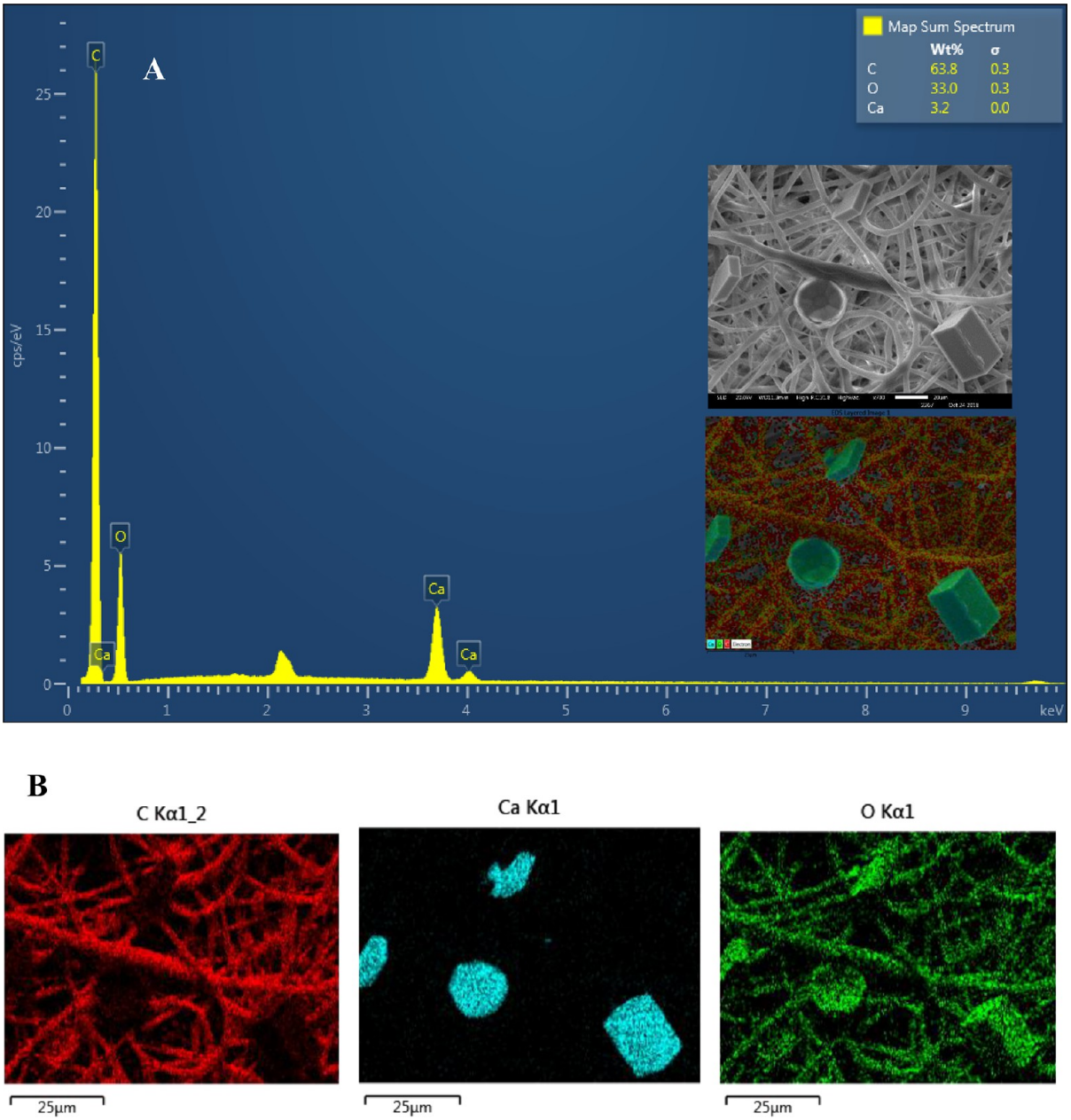

Figure 11. SEM-EDX of calcite and vaterite crystals grown on R-PCL fibers mesh (A) and major-element chemical composition of $CaCO_3$ crystals (B). Elements designations: C for carbon, Ca for calcium, and O for oxygen.

technique to characterize the roughness of PCL scaffolds. Our results show that the specific adsorption multipoint BET surface measurements on PR-PCL and PA-PCL fiber meshes were higher than that of the NP-PCL substrate in the range of 0.003 to 0.660 m^2/g, being larger for the PA-PCL fiber mesh of 0.660 m^2/g. Indeed, the BET surface of melted PCL showed 0 m^2/g with a pore volume of 0.001 mL/g. It is clear that specific adsorption BET surface values depend on the material type and dimensions. These BET surface values are less than standard CO_2 gas adsorption through PCL diffusion since here the CO_2 pressure is not considered under $CaCl_2$/TRIS buffered media in the GD technique. We believe that different ratio of $CO_2/CaCl_2$-TRIS-buffered media permeability has a key role in the kinetics of $CaCO_3$ crystallization and by this can conduct the crystallization of $CaCO_3$ toward a specific crystalline form. The precipitation of $CaCO_3$ in the GD crystallization method results from the diffusion of CO_2 vapor into the buffered $CaCl_2$ solution.[48] Therefore, it was found that by changing PCL topography and surface porosity, both calcite and vaterite polymorphs can be obtained. In general, the equilibrium concentration of dissolved CO_2 gas into PCL substrate (solubility) depends on polymer interaction and the availability of free volume for hole filling. It is known that differences in the solubility of specific gases in a particular polymer film determine which gas diffuses more readily cross that polymer film.[49] Also, permeability of the dissolved CO_2 gas penetrating through independent film and the flow of the gas per unit film area per unit time and the driving force (partial pressure difference) per unit film thickness are other important factors.[50] Then, surface properties of PCL fiber meshes, as templates in the mineralization of $CaCO_3$, e.g., distribution, diameter, pores

https://dx.doi.org/10.1021/acs.cgd.0c00803
Cryst. Growth Des. 2020, 20, 5610−5625

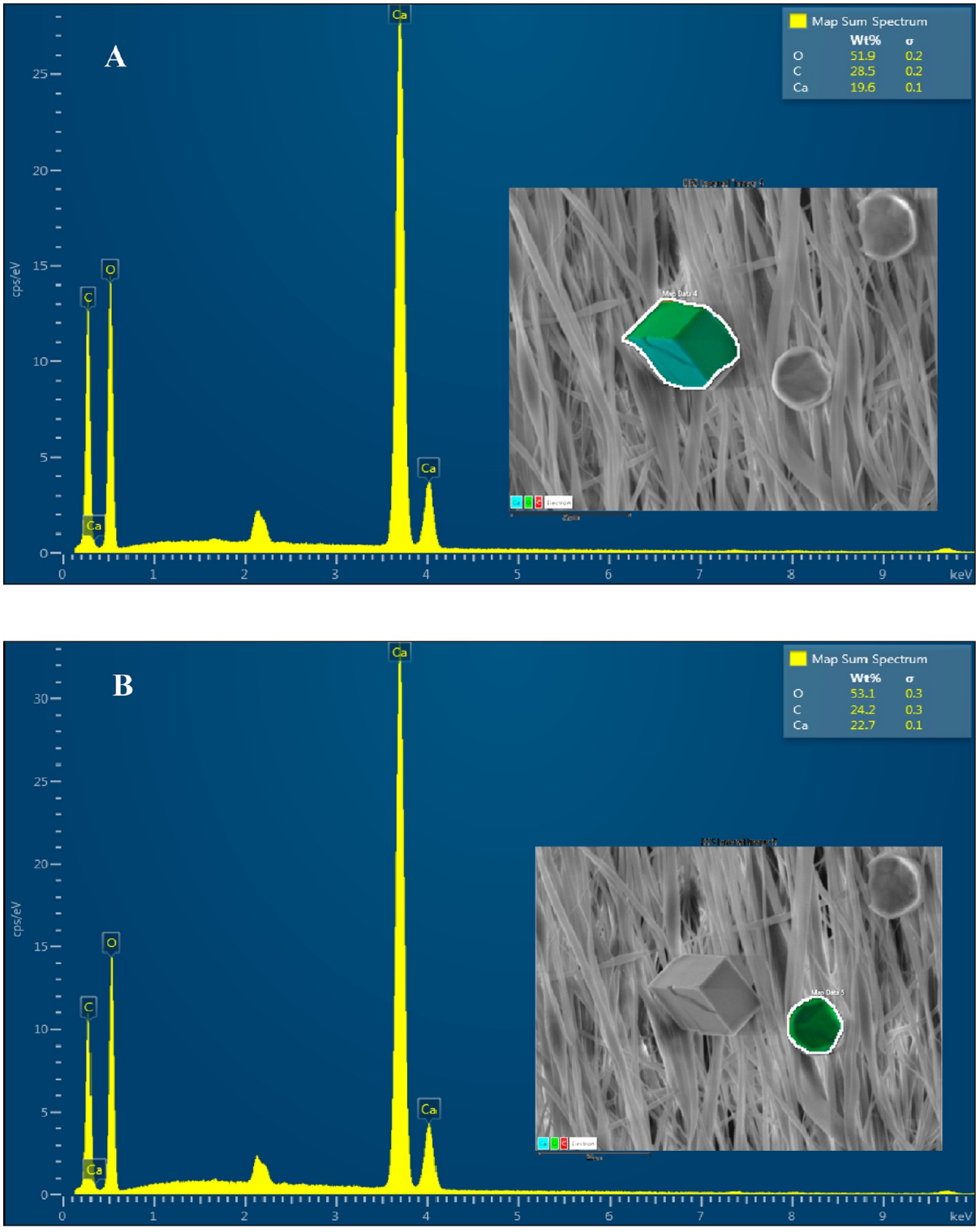

Figure 12. SEM-EDX of calcite (A) and vaterite (B) crystals grown on A-PCL fibers mesh. Elements designations: C for carbon, Ca for calcium, and O for oxygen.

sizes on PCL fibers as many other variables such as concentration, aging time, agitation, among others,[51] become a promising strategy for studying the effect of electrospun polymer templates in order to study the $CaCO_3$ polymorph occurrence and crystal growth. In addition, we provide multipoint BET, BJH adsorption/desorption summaries of different PCL substrates in Supporting Information (Table S1).

Figure 13 shows the XRD patterns of $CaCO_3$ crystals grown on glass, melted PCL and the nonporous and porous electrospun R-PCL and A-PCL fiber meshes obtained by using the GD crystallization method. The XRD spectrum of $CaCO_3$ obtained by using flat glass without PCL fibers (negative control) revealed that only calcite was formed (Figure 13 A). When melted PCL (positive control) was utilized as a solid template (Figure 13 B), the XRD

https://dx.doi.org/10.1021/acs.cgd.0c00803
Cryst. Growth Des. 2020, 20, 5610−5625

Table 1. Contact Angles at the Surface of All PCL Fiber Meshes[a]

PCL samples	contact angle [deg] H_2O	contact angle [°] $CaCl_2$/TRIS
control[1]	32.77 ± 3.34	52.19 ± 6.97
control[2]	62.96 ± 3.25	68.67 ± 7.35
R-PCL mesh	104.06 ± 2.92	107.86 ± 5.32
A-PCL mesh	115.88 ± 1.26	113.53 ± 4.28
PR-PCL mesh	119.31 ± 1.50	117.77 ± 2.75
PA-PCL mesh	113.53 ± 1.71	113.82 ± 1.65

[a]Control[1] and control[2] correspond to glass and melt PCL, respectively.

confirmed the formation of calcite as a unique type of crystal. Moreover, Figure 13B shows the typical very strong PCL reflection peaks at 2θ 21.4° and 23.7° indexed as (110) and (200) reflections as well as the reflection peak at 2θ = 22.3° indexed as (111).[52,53] However, XRD patterns of $CaCO_3$ obtained in the presence of nonporous and porous electrospun R-PCL and A-PCL fiber meshes (Figure 13C–F) clearly showed a crystalline peak ascribed at 2θ = 29.4° and 2θ = 28.3° indexed as (104) and (101) reflections confirming the polymorphs of calcite and vaterite, respectively. Indeed, a new reflection peak at 2θ = 31.6° corresponding to calcite is observed. When NP-PCL and P-PCL electrospun fiber meshes were used as a template instead of melted PCL film, the stabilization of less stable vaterite polymorph was

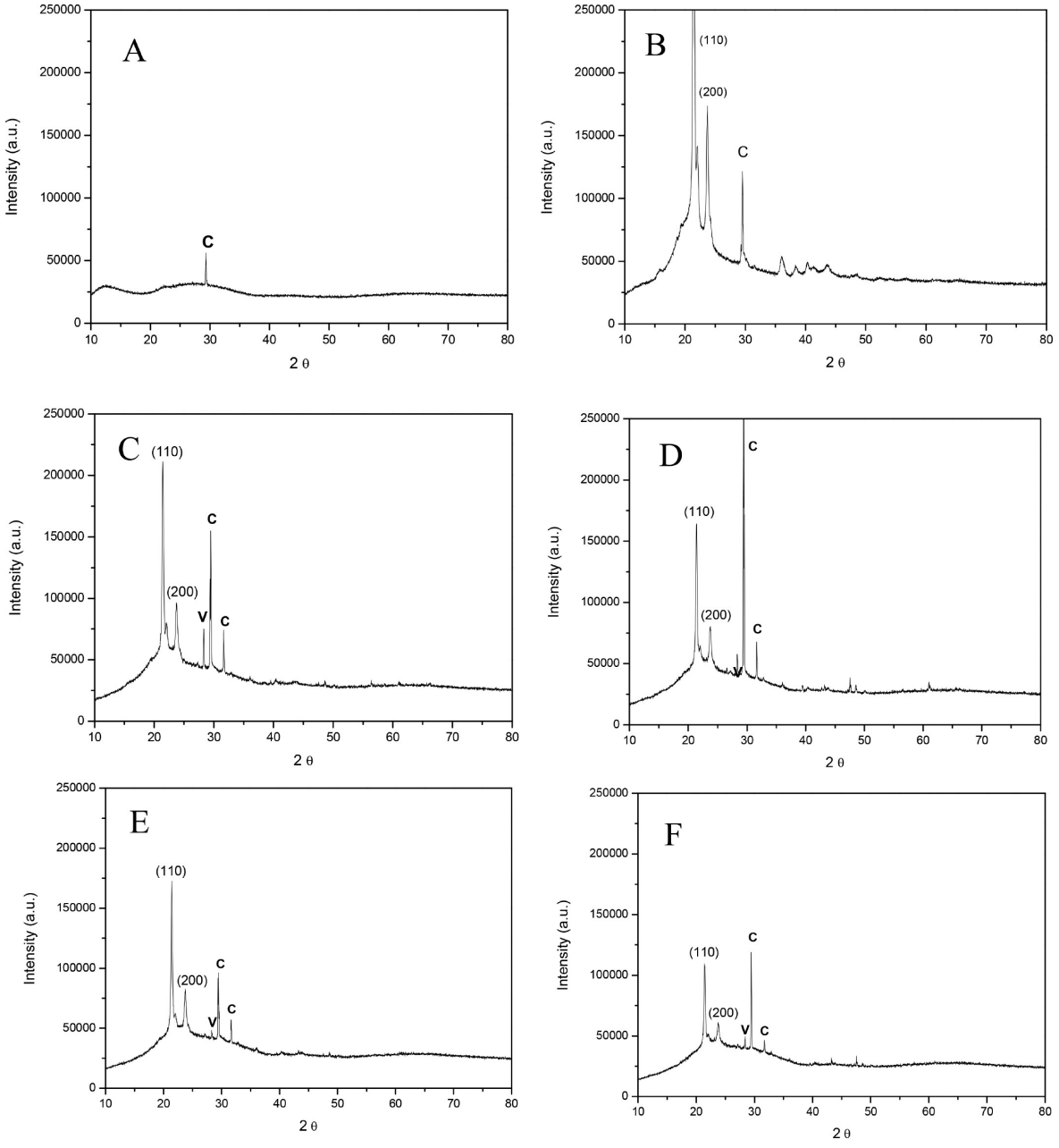

Figure 13. XRD patterns of $CaCO_3$ crystals grown on the surface of (A) glass, (B) melt PCL, (C) R-PCL fibers mesh, (D) A-PCL fibers meshes, (E) PR-PCL fibers mesh and (F) PA-PCL fibers mesh. Polymorphs designations: C for calcite and V for vaterite. Reflections (110) and (200) at 21.4° and 23.7° are from PCL in the XRD pattern.

https://dx.doi.org/10.1021/acs.cgd.0c00803
Cryst. Growth Des. 2020, 20, 5610–5625

obtained. In general, when nonporous and porous electrospun R-PCL and A-PCL fiber meshes were used as a solid template, XRD patterns of $CaCO_3$ particles showed different relative intensities of reflections peaks confirming the crystalline phases of calcite and vaterite (Figure 13C−D vs 13E−F). Surprisingly, XRD spectra of $CaCO_3$ obtained in the presence of PA-PCL fiber mesh (Figure 13D,F) show several crystalline peaks at 2θ = 36.0°, 39.4°, 43,2°, 47.5°, and 60.9°, confirming the polymorph of calcite. Indeed, a new reflection peak at 2θ 32.8° indexed as (006) corresponding to calcite was also observed.

4. CONCLUSIONS

We demonstrate that the distribution of PCL fibers affects the nucleation and polymorphism of $CaCO_3$ showing the capability to stabilize calcite and vaterite polymorphs. The presence of pores and the pore size in the PCL meshes with respect to NP-PCL fiber mesh affects the predominance of calcite/vaterite crystals and the intensities of the crystallographic faces in both polymorphs. We observed that the electrospun PCL meshes behave as low wettability systems with respect to glass and melted PCL controls. Moreover, the contact angle of NPA-PCL fibers was greater than NPR-PCL fibers in aqueous and crystallization liquid media, indicating a greater roughness of this substrate. Indeed, the A-PCL fibers with micrometric pores showed a smaller contact angle than R-PCL fiber with nanometric pores in both liquid media. Furthermore, the hydrophobic character of the PCL meshes varied with the change of topography and the presence of pores. The surface BET analysis allowed us to suggest that the presence of pores on PCL fibers changes their permeability with respect to the diffusion of CO_2 gas through penetration of PCL fibers template based on the ratio of $CO_2/CaCl_2$-TRIS-buffered media affecting the kinetics of $CaCO_3$ crystallization and may allow precipitation of a specific crystalline form. We are convinced that the use of electrospun polymer fibers with controlled-surface topography or containing a spatial charge arrangement as well as the presence of pores on the fiber surface as an organic electrospun polymer template represents an interesting approach to study various aspects of mineralization of $CaCO_3$ such as nucleation, crystal growth, and polymorphism delivering valuable tools to develop biomaterials based on $CaCO_3$ with potential industrial and biomedical uses.

■ ASSOCIATED CONTENT

Supporting Information

The Supporting Information is available free of charge at https://pubs.acs.org/doi/10.1021/acs.cgd.0c00803.

Details of synthesis and experimental procedure. Figures S1−S4. Experimental procedures for the GD crystallization of $CaCO_3$, electrospun meshes of aligned and random PCL fibers production, contact angle and surface BET measurements of the surface of PCL meshes (PDF)

■ AUTHOR INFORMATION

Corresponding Author

Andrónico Neira-Carrillo − *Department of Biological and Animal Science, University of Chile, 11735 Santiago, Chile;* orcid.org/0000-0003-0060-7518; Phone: +56-2-29785674; Email: aneira@uchile.cl; Fax: +56-2-29785526

Authors

Felipe Sepúlveda − *Department of Biological and Animal Science, University of Chile, 11735 Santiago, Chile*

Nicole Butto − *Department of Biological and Animal Science, University of Chile, 11735 Santiago, Chile*

José Luis Arias − *Department of Biological and Animal Science, University of Chile, 11735 Santiago, Chile*

Mehrdad Yazdani-Pedram − *Department of Organic and Physical Chemistry, University of Chile, 1007 Santiago, Chile*

Piotr K. Szewczyk − *International Centre of Electron Microscopy for Materials Science, Faculty of Metals Engineering and Industrial Computer Science, AGH University of Science and Technology, 30-059 Cracow, Poland;* orcid.org/0000-0003-1441-7387

Adam Gruszczynski − *International Centre of Electron Microscopy for Materials Science, Faculty of Metals Engineering and Industrial Computer Science, AGH University of Science and Technology, 30-059 Cracow, Poland*

Urszula Stachewicz − *International Centre of Electron Microscopy for Materials Science, Faculty of Metals Engineering and Industrial Computer Science, AGH University of Science and Technology, 30-059 Cracow, Poland;* orcid.org/0000-0001-5102-8685

Complete contact information is available at: https://pubs.acs.org/10.1021/acs.cgd.0c00803

Notes

The authors declare no competing financial interest.

■ ACKNOWLEDGMENTS

This work was supported by FONDECYT No. 1171520. U.S. thanks the National Science Centre in Poland for the Sonata Bis 5 project, No. 2015/18/E/ST5/00230 allowing this study, and a Ph.D. scholarship for P.K.S. The FIB-SEM imaging was supported by the infrastructure at the International Centre of Electron Microscopy for Materials Science (IC-EM) at AGH University of Science and Technology.

■ ABBREVIATIONS

PCL, polycaprolactone; $CaCO_3$, calcium carbonate; GD, gas diffusion

■ REFERENCES

(1) Lowenstam, H. A.; Weiner, S. *On Biomineralization*; Oxford University Press: New York, 1989.

(2) Estroff, L. A. Introduction: biomineralization. *Chem. Rev.* **2008**, *108*, 4329−4331.

(3) Heuer, A.; Fink, D.; Laraia, V.; Arias, J.; Calvert, P.; Kendall, K; Messing, G.; Blackwell, J; Rieke, P.; Thompson, D. Innovative materials processing strategies: a biomimetic approach. *Science* **1992**, *255*, 1098−1105.

(4) Aizenberg, J.; Weaver, J. C.; Thanawala, M. S.; Sundar, V. C.; Morse, D. E.; Fratzl, P. Skeleton of *Euplectella sp.*: structural hierarchy from the nanoscale to the macroscale. *Science* **2005**, *309*, 275−278.

(5) Sumper, M.; Brunner, E. Learning from diatoms: nature's tools for the production of nanostructured silica. *Adv. Funct. Mater.* **2006**, *16*, 17−26.

(6) Arias, J. L.; Fernandez, M. S. Biomimetic processes through the study of mineralized shells. *Mater. Charact.* **2003**, *50*, 189−195.

(7) Simkiss, K.; Wilbur, K. M. *Biomineralization: Cell Biology and Mineral Deposition*; Academic Press: San Diego, 1989.

(8) Mayer, G.; Sarikaya, M. Rigid biological composite materials: structural examples for biomimetic design. *Exp. Mech.* **2002**, *42*, 395−403.
(9) Mayer, G. Rigid biological systems as models for synthetic composites. *Science* **2005**, *310*, 1144−1147.
(10) Mann, S.; Ozin, G. A. Synthesis of inorganic materials with complex form. *Nature* **1996**, *382*, 313−318.
(11) Sumper, M.; Brunner, E. Silica biomineralisation in diatoms: The model organism *Thalassiosira pseudonana*. *ChemBioChem* **2008**, *9*, 1187−1194.
(12) Zhang, D. F.; Sun, L. D.; Zhang, J.; Yan, Z. G.; Yan, C. H. Hierarchical construction of ZnO architectures promoted by heterogeneous nucleation. *Cryst. Growth Des.* **2008**, *8*, 3609−3615.
(13) Dawlee, S.; Sugandhi, A.; Balakrishnan, B.; Labarre, D.; Jayakrishnan, A. Oxidized chondroitin sulfate-cross-linked gelatin matrixes: a new class of hydrogels. *Biomacromolecules* **2005**, *6*, 2040−2048.
(14) Arias, J. L.; Fernãndez, M. S. Polysaccharides and proteoglycans in calcium carbonate-based biomineralization. *Chem. Rev.* **2008**, *108*, 4475−4482.
(15) Meldrum, F. C. Calcium carbonate in biomineralisation and biomimetic chemistry. *Int. Mater. Rev.* **2003**, *48*, 187−224.
(16) Cölfen, H. Precipitation of carbonates: recent progress in controlled production of complex shapes. *Curr. Opin. Colloid Interface Sci.* **2003**, *8*, 23−31.
(17) Nys, Y.; Hincke, M. T.; Arias, J. L.; Garcia-Ruiz, J. M.; Solomon, S. E. Avian eggshell mineralization. *Poult. Avi. Biol. Rev.* **1999**, *10*, 143−166.
(18) Sun, S.; Mao, L. B.; Lei, Z.; Yu, S. H.; Cölfen, H. Hydrogels from amorphous calcium carbonate and polyacrylic acid: bio-inspired materials for "mineral plastics. *Angew. Chem., Int. Ed.* **2016**, *55*, 11765−11769.
(19) Krishna Pai, R.; Pillai, S. Water-soluble terpolymer directs the hollow triangular cones of packed calcite needles. *Cryst. Growth Des.* **2007**, *7*, 215−217.
(20) Balthasar, U.; Cusack, M. Aragonite-calcite seas-Quantifying the gray area. *Geology* **2015**, *43*, 99−102.
(21) Boyjoo, Y.; Pareek, V. K.; Liu, J. Synthesis of micro and nano-sized calcium carbonate particles and their applications. *J. Mater. Chem. A* **2014**, *2*, 14270−14288.
(22) Grasby, S. E. Naturally precipitating vaterite (μ-$CaCO_3$) spheres: unusual carbonates formed in an extreme environment. *Geochim. Cosmochim. Acta* **2003**, *67*, 1659−1666.
(23) Krishna Pai, R.; Pillai, S. Divalent cation-induced variations in polyelectrolyte conformation and controlling calcite morphologies: Direct observation of the phase transition by atomic force microscopy. *J. Am. Chem. Soc.* **2008**, *130*, 13074−13078.
(24) Mann, S. *Biomineralization: Principles and Concepts in Bioinorganic Materials Chemistry*; Oxford University Press on Demand: New York, 2001; Vol. *5*.
(25) Beato, C.; Fernández, M. S.; Fermani, S.; Reggi, M.; Neira-Carrillo, A.; Rao, A.; Falini, G.; Arias, J. L. Calcium carbonate crystallization in tailored constrained environments. *CrystEngComm* **2015**, *17*, 5953−5961.
(26) Wesson, J. A.; Ward, M. D. Pathological biomineralization of kidney stones. *Elements* **2007**, *3*, 415−421.
(27) Rao, A.; Vãsquez-Quitral, P.; Fernández, M. S.; Berg, J. K.; Sãnchez, M.; Drechsler, M.; Neira-Carrillo, A.; Arias, J. L.; Gebauer, D.; Cölfen, H. pH-dependent schemes of calcium carbonate formation in the presence of alginates. *Cryst. Growth Des.* **2016**, *16*, 1349−1359.
(28) Fratzl, P. Biomimetic materials research: what can we really learn from nature's structural materials? *J. R. Soc., Interface* **2007**, *4*, 637−642.
(29) Estroff, L. A.; Hamilton, A. D. At the interface of organic and inorganic chemistry: Bioinspired synthesis of composite materials. *Chem. Mater.* **2001**, *13*, 3227−3235.
(30) Saveleva, M.; Prikhozhdenko, E.; Gorin, D.; Skirtach, A. G.; Yashchenok, A.; Parakhonskiy, B. Polycaprolactone-based, porous $CaCO_3$ and Ag nanoparticle modified scaffolds as a SERS platform with molecule-specific adsorption. *Front. Chem.* **2020**, *7*, 1−11.
(31) Savelyeva, M. S.; Abalymov, A. A.; Lyubun, G. P.; Vidyasheva, I. V.; Yashchenok, A. M.; Douglas, T. E.; Gorin, D. A.; Parakhonskiy, B. V. Vaterite coatings on electrospun polymeric fibers for biomedical applications. *J. Biomed. Mater. Res., Part A* **2017**, *105*, 94−103.
(32) Ivanova, A. A.; Syromotina, D. S.; Shkarina, S. N.; Shkarin, R.; Cecilia, A.; Weinhardt, V.; Baumbach, T.; Saveleva, M. S.; Gorin, D. A.; Douglas, T. E. L.; Parakhonskiy, B. V.; Skirtach, A. G.; Cools, P.; De Geyter, N.; Morent, R.; Oehr, C.; Surmeneva, M. A.; Surmenev, R. A. Effect of low-temperature plasma treatment of electrospun polycaprolactone fibrous scaffolds on calcium carbonate mineralization. *RSC Adv.* **2018**, *8*, 39106−39114.
(33) Saveleva, M. S.; Ivanov, A. N.; Kurtukova, M. O.; Atkin, V. S.; Ivanova, A. G.; Lyubun, G. P.; Martyukova, A. V.; Cherevko, E. I.; Sargsyan, A. K.; Fedonnikov, A. S.; Norkin, I. A.; Skirtach, A. G.; Gorin, D. A.; Parakhonskiy, B. V. Hybrid PCL/$CaCO_3$ scaffolds with capabilities of carrying biologically active molecules: synthesis, loading and in vivo applications. *Mater. Sci. Eng., C* **2018**, *85*, 57−67.
(34) Svenskaya, Y. I.; Fattah, H.; Inozemtseva, O. A.; Ivanova, A. G.; Shtykov, S. N.; Gorin, D. A.; Parakhonskiy, B. V. Key Parameters for size- and shape-controlled synthesis of vaterite particles. *Cryst. Growth Des.* **2018**, *18*, 331−337.
(35) Neira, C. A.; Fernandez, M. S.; Retuert, J.; Arias, J. L. Effect of the crystallization chamber design on the polymorphs of calcium carbonate using the sitting-drop method. In Architecture and Application of Biomaterials and Biomolecular Materials; Barron, A. E., Klok, H.-A., Deming, T. J., Eds.; Mater. Res. Soc. Symp. Proc., 2004, EXS-1, pp 321−326.
(36) Weiner, S.; Dove, P. M. An overview of biomineralization processes and the problem of the vital effect. *Rev. Mineral. Geochem.* **2003**, *54*, 1−29.
(37) Fernández, M. S.; Montt, B.; Neira-Carrillo, A.; Arias, J. L. Effect of carbonic anhydrase immobilized on eggshell membranes on calcium carbonate crystallization *in vitro*. In *Biomineralization - From Molecular and Nano-structural Analyses to Environmental Science*; Endo, K.; Kogure, T.; Nagasawa, H., Eds.; Springer-Verlag Tokio Book, 2018; Chapter 4, pp 31−37. .
(38) Dominguez-Vera, J. M.; Gautron, J.; Garcia-Ruiz, J. M.; Nys, S. The effect of avian uterine fluid on the growth behavior of calcite crystals. *Poult. Sci.* **2000**, *6*, 901−907.
(39) Neira-Carrillo, A.; Retuert, J.; Martínez, F.; Arias, J. L. Effect of crosslinked chitosan as a constrained volume on the in vitro calcium carbonate crystallization. *J. Chil. Chem. Soc.* **2008**, *53*, 1367−1372.
(40) Neira-Carrillo, A.; Acevedo, D. F.; Peralta, D. O.; Barbero, C.; Cölfen, H.; Arias, J. L. Influence of conducting polymers based on carboxylated polyaniline on in vitro $CaCO_3$ crystallization. *Langmuir* **2008**, *24*, 12496−12507.
(41) Neira-Carrillo, A.; Krishna Pai, R.; Fernández, M. S.; Carreño, E.; Vasquez-Quitral, P.; Arias, J. L. Synthesis and characterization of sulfonated polymethylsiloxane polymer as template for crystal growth of $CaCO_3$. *Colloid Polym. Sci.* **2009**, *287*, 385−393.
(42) Stachewicz, U.; Szewczyk, P. K.; Kruk, A.; Barber, A. H.; Czyrska-Filemonowicz, A. Pore shape and size dependence on cells growth into electrospun fiber scaffolds for tissue engineering: 2D and 3D analyses using SEM and FIB-SEM tomography. *Mater. Sci. Eng., C* **2019**, *95*, 397−408.
(43) Cherpinski, A.; Szewczyk, P. K.; Gruszczyński, A.; Stachewicz, U.; Lagaron, J. M. Oxygen-scavenging multilayered biopapers containing palladium nanoparticles obtained by the electrospinning coating technique. *Nanomaterials* **2019**, *9*, 262.
(44) Shoja, M.; Kamyar, S.; Ahmad, M. B.; Zakaria, Z. Preparation and characterization of poli (ϵ-caprolactone)/TiO_2 micro-composites. *Dig. J. Nanomater. Bios.* **2005**, *10*, 471−477.
(45) Szewczyk, P. K.; Ura, D. P.; Metwally, S.; Knapczyk-Korczak, J.; Gajek, M.; Marzec, M. M.; Bernasik, A.; Stachewicz, U.

https://dx.doi.org/10.1021/acs.cgd.0c00803
Cryst. Growth Des. 2020, 20, 5610−5625

Roughness and fibers fraction dominated wetting of electrospun fiber based porous meshes. *Polymers* **2019**, *11*, 34.
(46) Metwally, S.; Karbowniczek, J. E.; Szewczyk, P. K.; Marzec, M. M.; Gruszczyński, A.; Bernasik, A.; Stachewicz, U. Single-step approach to tailor surface chemistry and potential on electrospun PCL fibers for tissue engineering application. *Adv. Mater. Interfaces* **2019**, *6*, 1801211.
(47) Ivanova, A. A.; Syromotina, D. S.; Shkarina, S. N.; Shkarin, R.; Cecilia, A.; Weinhardt, V.; Baumbach, T.; Saveleva, M. S.; Gorin, D. A.; Douglas, T. E. L.; Parakhonskiy, B. V.; Skirtach, A. G.; Cools, P.; De Geyter, N.; Morent, R.; Oehr, C.; Surmeneva, M. A.; Surmenev, R. A. Effect of low-temperature plasma treatment of electrospun polycaprolactone fibrous scaffolds on calcium carbonate mineralisation. *RSC Adv.* **2018**, *8*, 39106−39114.
(48) Arias, J. I.; Jure, C.; Wiff, J. P.; Fernández, M. S.; Fuenzalida, V.; Arias, J. L. Effect of sulfate content of biomacromolecules on the crystallization of calcium carbonate. In: Advanced biomesherials − characterization, tissue engineering and complexity; Moss, S.C., Ed.; *Mesh. Res. Soc. Symp. Proc.* 2002, *711*, 243−248.
(49) Pino, M.; Duckett, R. A.; Ward, I. M. Single and mixed gas diffusion through polyethylene films. *Polymer* **2005**, *46*, 4882−4890.
(50) Ashley, R. J. Permeability and plastics packaging. In *Polymer Permeability*; Comyn, J., Ed.; Elsevier: New York; 1985, pp 269−308.
(51) Wang, L.; Sondi, I.; Matijevicô, E. *J. Colloid Interface Sci.* **1999**, *218*, 545−553.
(52) Jana, S.; Leung, M.; Chang, J.; Zhang, M. Effect of nano-and micro-scale topological features on alignment of muscle cells and commitment of myogenic differentiation. *Biofabrication* **2014**, *6*, 035012.
(53) Li, X.; Liu, H.; Wang, J.; Li, C. Preparation and characterization of poly(3-caprolactone) nonwoven mats via melt electrospinning. *Polymer* **2012**, *53*, 248−253.

https://dx.doi.org/10.1021/acs.cgd.0c00803
Cryst. Growth Des. 2020, 20, 5610−5625